minerals

MDPI

Article

High-Resolution Transmission Electron Microscopy Study of a Powder River Basin Coal-Derived Fly Ash

James C. Hower [1,2,*], Debora Berti [3], Christopher R. Winkler [4], Dali Qian [1,5] and Nicolas J. Briot [5]

1 Center for Applied Energy Research, University of Kentucky, 2540 Research Park Drive, Lexington, KY 40511, USA; dali.qian@uky.edu
2 Department of Earth & Environmental Sciences, University of Kentucky, Lexington, KY 40506, USA
3 Department of Oceanography, Texas A&M University, College Station, TX 77843, USA; deborasm74@runbox.com
4 Analytical Instrumentation Facility, North Carolina State University, Raleigh, NC 27695, USA; crwinkler@ncsu.edu
5 Electron Microscopy Center, University of Kentucky, Lexington, KY 40506, USA; nicolas.briot@uky.edu
* Correspondence: james.hower@uky.edu; Tel.: +1-859–257-0261

Abstract: Examination of a fly ash derived from the combustion of a low-S, subbituminous Powder River Basin coal by Scanning Electron Microscopy (SEM) and High-resolution Transmission Electron Microscopy (HRTEM), both supplemented by Energy-dispersive X-ray spectroscopy (EDS), showed that the fly ashes were dominated by amorphous phases, Ca-rich plagioclase feldspars, Mg-rich phases, complex Ca-Mg-Al-Si-Ti-Fe grains, and trace amounts of REE-rich particles. Many of the particles were rimmed by a Ca-S, possibly a sulfate. HRTEM-EDS examination of a REE-rich particle proved it to be a mix of light- and heavy-rare earth minerals mixed with amorphous phases.

Keywords: class C fly ash; lanthanides; subbituminous coal; calcium

check for updates

Citation: Hower, J.C.; Berti, D.; Winkler, C.R.; Qian, D.; Briot, N.J. High-Resolution Transmission Electron Microscopy Study of a Powder River Basin Coal-Derived Fly Ash. *Minerals* **2022**, *12*, 975. https://doi.org/10.3390/min12080975

Academic Editors: Scott N. Montross, Bruce Folkedahl and Jonathan Yang

Received: 9 July 2022
Accepted: 29 July 2022
Published: 30 July 2022

1. Introduction

Over the past three decades, low-S, subbituminous Powder River Basin (PRB; encompassing parts of Wyoming and Montana) coal has penetrated the coal-fired utility markets in the United States, displacing high-S Illinois Basin coal, medium-S Central Appalachian coal in some southeastern US markets, and mine-mouth lignite at Texas power plants. The transition from the relatively local sources, though not without problems and expenses in the conversions of boilers to the combustion of the low-heating value subbituminous coal, was driven by a combination of factors, including SO_2-emission regulations [1], the anticipation and ultimate enactment of toxic-element-emission guidelines [2], the low cost of mining the thick coal, and the rail network able to move the coal to the customers [3–13].

While searching for high-Rare Earth Element (REE) fly ashes as potential targets for REE extraction, Taggart et al. [14] and Hood et al. [15] examined ashes derived from the combustion of PRB coal (also see Bagdonas et al. [16]). Ultimately, while those fly ashes showed a better potential for extraction of the REE than high volatile bituminous Central Appalachian coal-derived ashes [14], the subsequent bench- and pilot-scale studies were on the higher-REE-content Central Appalachian-derived ashes [17–20].

Scanning electron microscopy (SEM) and high-resolution transmission electron microscopy (HRTEM) studies of the Central Appalachian coal-derived fly ashes have been conducted to determine the modes of occurrence of REE in those class F (high Fe vs. high Ca for class C fly ashes; following [21]) fly ashes [15,17,22–24]. Aside from the Transmission electron microscopy (TEM) portion of the Hood et al. [15] study and the inclusion of PRB-derived fly ashes in the comparison of normalized-REE-distribution signatures from the Central Appalachian, Illinois, and Powder River basins, the PRB-derived fly ashes have been largely overlooked in our studies. Considering the extensive coal-fired utility

utilization of PRB coal throughout much of the United States and how much fly ash is produced annually, this is a regrettable oversight. In this short discussion, we turn attention to the fine structure of PRB-coal-derived fly ashes.

2. Methods and Materials

2.1. Scanning and Transmission Electron Microscopy

Fly ash sample 93927, obtained from a Midwestern US power plant burning Powder River Basin coal, was originally prepared as 2.54-cm-diameter epoxy-bound pellet prepared to a final 0.05-µm-alumina polish for petrographic examination at the University of Kentucky Center for Applied Energy Research (CAER). A slice of the pellet was used for the scanning electron microscopy (SEM) examination at Virginia Tech's NanoEarth facility in Blacksburg, VA, USA. Following procedures established in similar studies [15,24], the SEM sample was coated with Au-Pd to prevent charging and observed using a FEI Quanta 600 field emission SEM in backscatter electron (BSE) mode to identify particles with high average atomic numbers. High BSE intensity particles were examined using Energy-dispersive spectroscopy (EDS) analyses on a Bruker-AXS XFlash silicon drift detector. EDS analyses were conducted at 20 keV, a sufficient overvoltage to detect diagnostic energy peaks of REE and achieve a spatial resolution of approximately 2 µm, with an X-ray range of 7–9 µm.

Based on the SEM-EDS analyses, a FEI Helios 600 NanoLab Focused Ion Beam (FIB) (TheroFisher, Waltham, MA USA) was used to extract and lift out a thin slice of the promising REE-rich mineral and/or glass assemblage tentatively identified as by SEM-EDS. The slice was mounted on a Cu grid and ion milled to approximately 100-nm thickness. Transmission electron microscopy (TEM) was conducted on a JEOL JEM-2100 analytical electron microscope (JEOL Ltd., Tokyo, Japan), with a LaB_6 electron gun, operated at 200 keV and equipped with a JEOL 60 mm^2 window silicon drift detector (SDD) based EDS system for chemical mapping at a spatial resolution of 3–20 nm. Selected area electron diffraction (SAED) was employed for mineralogical identification of grains. In conjunction with SAED and for grains too small for SAED, High Resolution TEM (HRTEM) was also used for mineral identification. Lattice spacings observed by HRTEM were measured from the corresponding diffractions patterns using the Gatan Microscopy Suite® image analysis software (Gatan, Inc., Pleasanton, CA, USA).

Further imaging and EDS characterizations were performed on the FIB slice noted above on a FEI Talos F200X TEM operating at 200 keV at the University of Kentucky Electron Microscopy Center. The EDS scans of areas of interest (4000–8000 eV) were examined by plotting the data with SigmaPlot version 14.5 and selecting energy (eV) and count ranges for enhancement. The complete EDS data is on Table S1. Fast Fourier transform (FFT) was used to determine the crystalline structure of the sub-micron grains.

2.2. Chemistry

Moisture, ash, and carbon analyses (the latter from the ultimate analysis) were conducted at the CAER following the ASTM D3176 [25]. Major oxides and non-REE minor element concentrations were quantified on a Rigaku ZSX Primus IV X-ray fluorescence unit at the CAER.

3. Results and Discussion

3.1. SEM-EDS

Considering the chemistry of the selected class C PRB-coal-derived versus class F Central Appalachian-coal-derived fly ashes (Table 1; following ASTM C618 classifications [21]), as expected, it is seen that the class C ashes have a higher CaO and lower Al_2O_3 + SiO_2 than the class F fly ashes. This difference ultimately impacts the behavior of the fly ashes with respect to the extraction of REE. As noted above, Taggart et al. [14] demonstrated that class C ashes had a higher percent of extractable REE than class F ashes.

Table 1. Comparison the fly ash chemistry for Powder River Basin (PRB) coal-derived and Central Appalachian (CAPP) coal-derived fly ashes. Data from University of Kentucky Center for Applied Energy Research studies. bdl—below detection limit.

		As Rec. (%)	Dry (%)	Ash Basis (%)									
Type	**Sample**	**Mois**	**C**	**Na_2O**	**MgO**	**Al_2O_3**	**SiO_2**	**P_2O_5**	**K_2O**	**CaO**	**TiO_2**	**Fe_2O_3**	**SO_3**
PRB	93925	0.13	3.68	2.11	6.04	17.82	36.43	1.27	0.41	26.28	1.18	5.44	1.40
PRB	93927	0.15	2.85	1.99	6.98	16.56	29.49	1.57	0.32	31.10	1.12	4.80	3.93
PRB	93966	0.08	2.63	1.67	4.21	22.53	38.30	1.37	0.57	22.94	1.30	5.21	1.12
PRB	93971	0.19	2.91	1.15	7.79	15.28	30.12	1.17	0.32	33.64	1.11	4.40	3.35
PRB	93973	0.11	2.70	1.55	5.08	20.67	39.20	0.97	0.55	22.44	1.19	5.98	1.37
CAPP	93814	0.13	0.15	0.09	0.81	30.27	55.27	0.04	2.13	0.93	1.51	8.41	bdl
CAPP	93819	0.11	0.46	0.07	0.90	32.93	54.38	0.06	2.35	1.03	1.57	6.24	bdl
CAPP	93914	0.79	8.33	0.27	1.22	29.61	51.84	0.37	2.35	1.83	1.42	11.00	0.42
CAPP	93932	0.17	7.76	0.32	1.07	28.43	54.21	0.54	2.26	4.01	1.60	7.60	0.09
CAPP	93955	0.22	8.11	0.25	0.94	30.76	52.81	0.52	1.90	1.72	1.75	7.54	0.12
CAPP	93963	0.13	7.82	0.38	1.05	26.50	52.08	0.36	2.52	2.05	1.48	14.06	0.14
CAPP	94012	bdl	6.48	0.29	1.16	29.89	52.64	1.36	2.44	2.04	1.59	8.41	0.22

		Ash Basis (ppm)							
Type	**Sample**	**V**	**Cr**	**Mn**	**Co**	**Ni**	**Cu**	**Zn**	**As**
PRB	93925	215	33	98	39	48	164	133	bdl
PRB	93927	192	26	80	34	39	181	96	2
PRB	93966	323	59	92	51	58	204	152	9
PRB	93971	185	25	50	58	43	174	106	bdl
PRB	93973	258	54	189	52	65	159	161	5
CAPP	93814	434	148	198	40	122	130	156	63
CAPP	93819	493	177	149	37	134	169	207	125
CAPP	93914	528	178	215	51	148	143	284	194
CAPP	93932	486	156	223	82	137	181	177	73
CAPP	93955	622	203	132	75	147	271	183	218
CAPP	93963	490	161	213	64	131	178	170	160
CAPP	94012	496	182	149	67	142	190	206	320

		Ash Basis (ppm) (Hg—Whole Sample Basis (ppm))								
Type	**Sample**	**Rb**	**Sr**	**Zr**	**Mo**	**Cd**	**Sb**	**Ba**	**Hg**	**Pb**
PRB	93925	190	2863	347	6	2	4	5984	0.86	60
PRB	93927	170	3151	335	bdl	2	3	6650	0.02	63
PRB	93966	63	3279	354	31	2	4	5634		84
PRB	93971	64	2864	314	bdl	2	2	5915		82
PRB	93973	76	2674	323	17	1	2	4972		83
CAPP	93814	62	845		59	1	bdl	963		75
CAPP	93819	26	1120		74	1	bdl	1010		113
CAPP	93914	113	1812		39	1	2	998	1.01	121
CAPP	93932	355	1175	302	152	1	6	1273		81
CAPP	93955	bdl	1035	327	122	bdl	bdl	1573	1.36	149
CAPP	93963	211	1581	345	110	3	9	1444	0.23	112
CAPP	94012	bdl	1767	296	117	bdl	6	2112		183

The mineralogical composition of any fly ash depends on the final temperature of the melted ash, the chemistry of the melted ash, the potential for interaction between the phases, and the rate of cooling of the melt. If the quenching is too rapid non-crystalline phases may be present. Mullite, anorthite, and other Al-Si-rich or Ca-rich minerals can crystallize from the melt or can result from solid-state reactions [26]. Within the CaO-Al_2O_3-SiO_2 system, the crystallization of anorthite, the Ca-rich plagioclase feldspar, versus mullite in the 1200–1300 °C range, the latter being more common in class F fly ashes, depends upon the balance between Al_2O_3 and CaO [27–29]. The Ca > > Na mineral with abundant Al and Si shown on Figure 1 is likely to be a plagioclase feldspar. If the counts per second

for Ca and Na represent the feldspar, with an ca. 5:1 Ca:Na ratio, the mineral would be bytownite. Within the temperature range of the cooling melts, diopside, a possible mineral site for the Mg (and some of the Ca) detected in the EDS, and plagioclase can co-exist in the diopside-forsterite-anorthite-albite compositional range [28,30]. If this, or another Ca-bearing mineral, is contributing to the EDS spectrum, the estimate of the plagioclase composition would change.

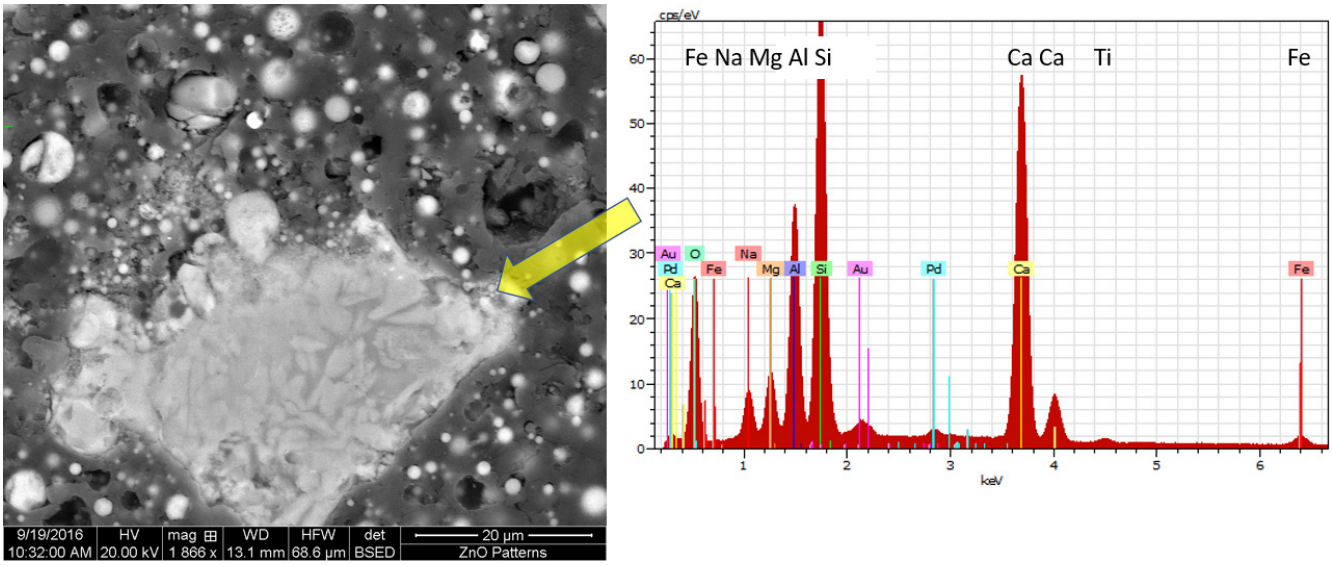

Figure 1. Plagioclase feldspar (bytownite or anorthite), possibly with other minerals, in sample 93927 (PRB-coal-derived fly ash). Left/Back-scatter image of fly ash. Scale = 20 µm. Right/EDS spectrum of elemental composition of large particle. Signals for Au and Pd are extraneous to the sample. Modified after Hood et al. [15].

A spherical Ca-Mg-Al-Si-Ti-Fe grain, a similar composition to the mineral assemblage in Figure 1, is shown in Figure 2. All of the figures are examples from sample 93927, the PRB-coal-derived fly ash. The bladed portions of the grains suggest a crystalline habit, much as Fe-rich spinels and mullite take on a crystalline form in class F fly ashes. In contrast to the latter grain, the bright particle illustrated on Figure 3 is dominated by Fe-oxides with lesser concentrations of Ca, Mg, Al, and Si. Several grains reminiscent of both Figures 2 and 3 particles are seen in the broader composite image (Figure 4), indicating that a complex variety of minerals and cryptocrystalline forms are present within the fly ash. Querol et al. [31], as summarized by Hower et al. [32] and shown in part by Ehlers [28], p. 74, discussed the transformation of minerals with an increase in temperature. Included in those transformations are the reactions of silicon spinel ($Al_2O_3{\cdot}3SiO_2$) + CaO to form gehlenite ($Ca_2Al_2SiO_7$) + SiO_2 at 950–1100 °C and gehlenite + SiO_2 to form anorthite + CaO at 1200–1400 °C in high-CaO melts and, with abundant Fe_2O_3, silicon spinel + Fe_2O_3 + CaO + SiO_2 reacting to form the clinopyroxene esseneite ($Ca(Al_{0.6}Fe_{14})SiO_6$) at 950–1100 °C and esseneite reacting with Al_2O_3 from glass to form anorthite + Fe_2O_3 in glass at 1400 °C. Above 1400 °C, Al, Si, and Ca can be incorporated into spinel minerals. We note that while the latter discussion revolves around the heating of coal-borne minerals and their progressive transformations, and notwithstanding the potential for some minerals to survive a total phase transformation or melting at the boiler temperatures (after all, partially melted, but not combusted, coal is observed in some fly ashes), of greater interest is the precipitation of minerals from the >1400 °C melt.

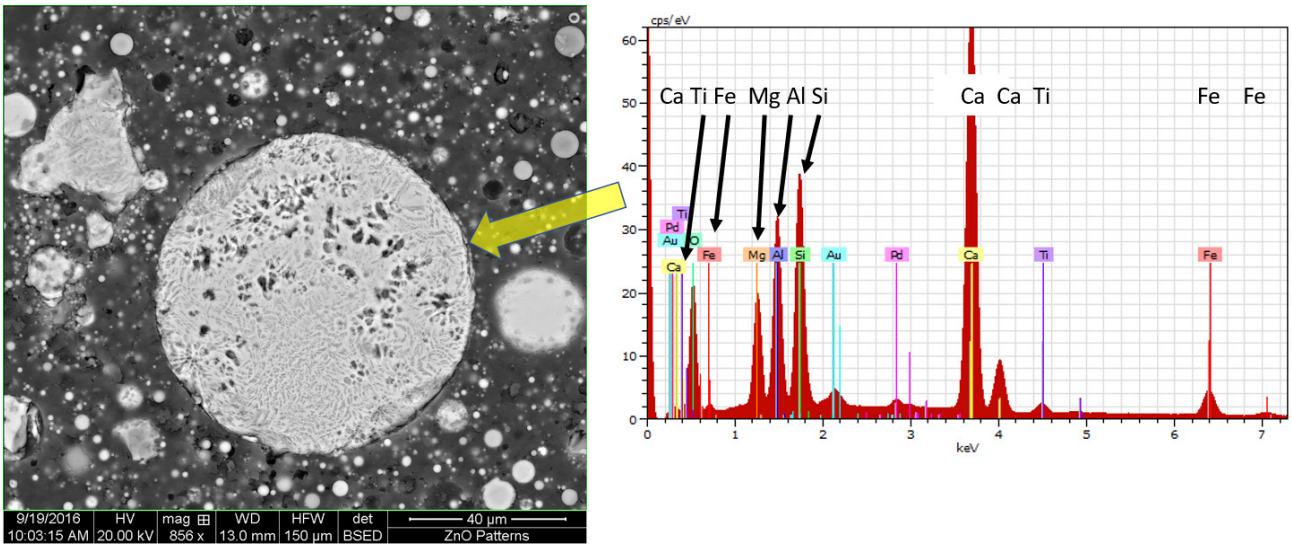

Figure 2. Left/Back-scatter image of Ca-Mg-Al-Si-Ti-Fe grain. Scale = 40 µm. Right/EDS spectrum of elemental composition of large particle. Signals for Au and Pd are extraneous to the sample.

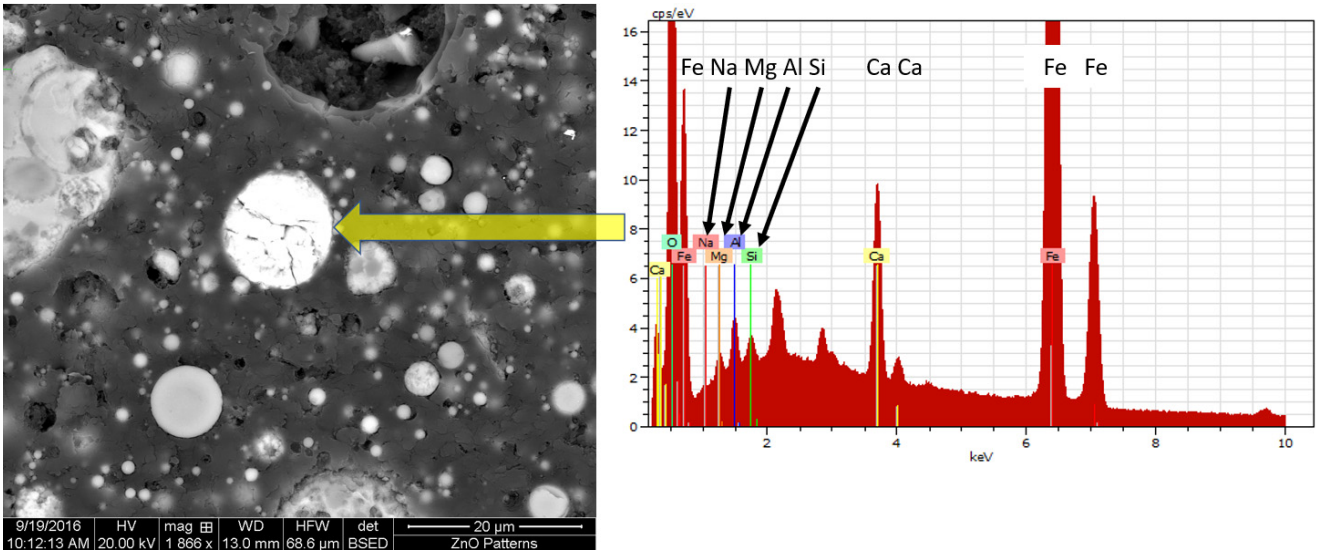

Figure 3. Left/Back-scatter image of Fe-rich grain. Scale = 20 µm. Right/EDS spectrum of elemental composition of large particle. Signals for Au and Pd (not labeled on this figure; see Figures 1 and 2) are extraneous to the sample.

Some REE-bearing fly ash particles have been found, as illustrated by Figure 5. In this case, a bright, spherical particle has an Al ≈ Si > Ca > Ba > Mg > P ≈ Nd > Sm ≈ Fe composition. If the Nd and Sm signals are real, it is likely that other REE, particularly La and Ce, are present but are obscured by the Ba Lα and Lβ peaks.

3.2. HRTEM

3.2.1. REE-Lean Particle: Analysis at Virginia Tech NanoEarth

HRTEM examination of a rounded particle shows that it is cored by an amorphous Ca > Al > >P ≈ Mg ≈ Si > S > Ti mix and rimmed by a largely Ca-S sulfate (?) (Figures 6 and 7). The concentrations of Mg, Si, P, and Ti (Figures 7 and 8) are lower than Ca, Al, and S (Figures 6 and 8), but there is a hint that Mg only mimics the Ca distribution in the particle core, not the rim. Titanium follows a similar distribution to Mg. Both Si and P partially

follow the rim's Ca-S distribution, particularly with the protrusion in the lower-left corner of the Figure 6 image.

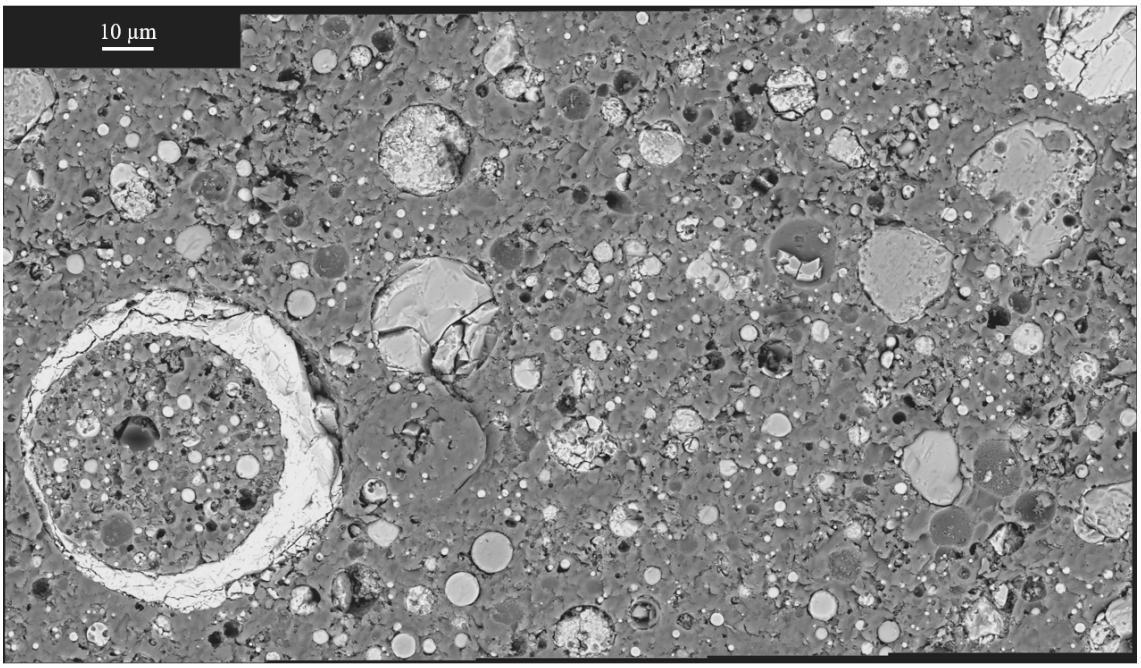

Figure 4. Back-scatter image of a large swath of the epoxy-bound pellet. Scale = 10 µm.

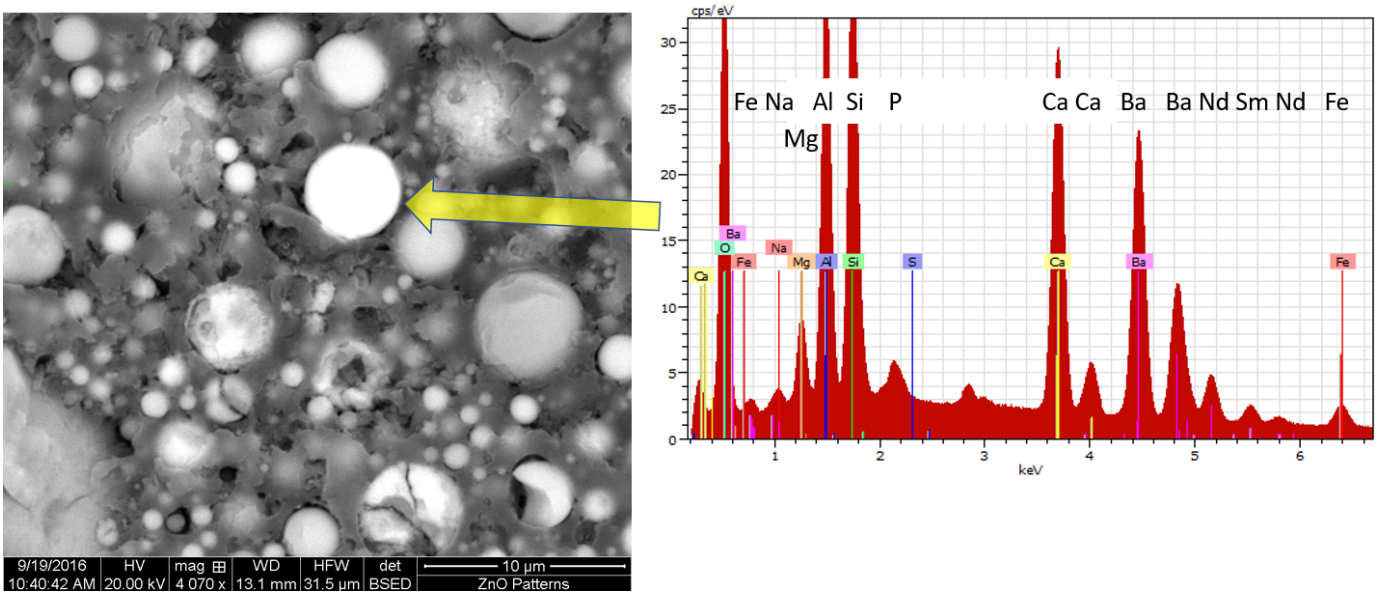

Figure 5. Left/Back-scatter image of REE-bearing grain. Scale = 10 µm. Right/EDS spectrum of elemental composition of large particle. Signals for Au and Pd (not labeled on this figure; see Figures 1 and 2) are extraneous to the sample.

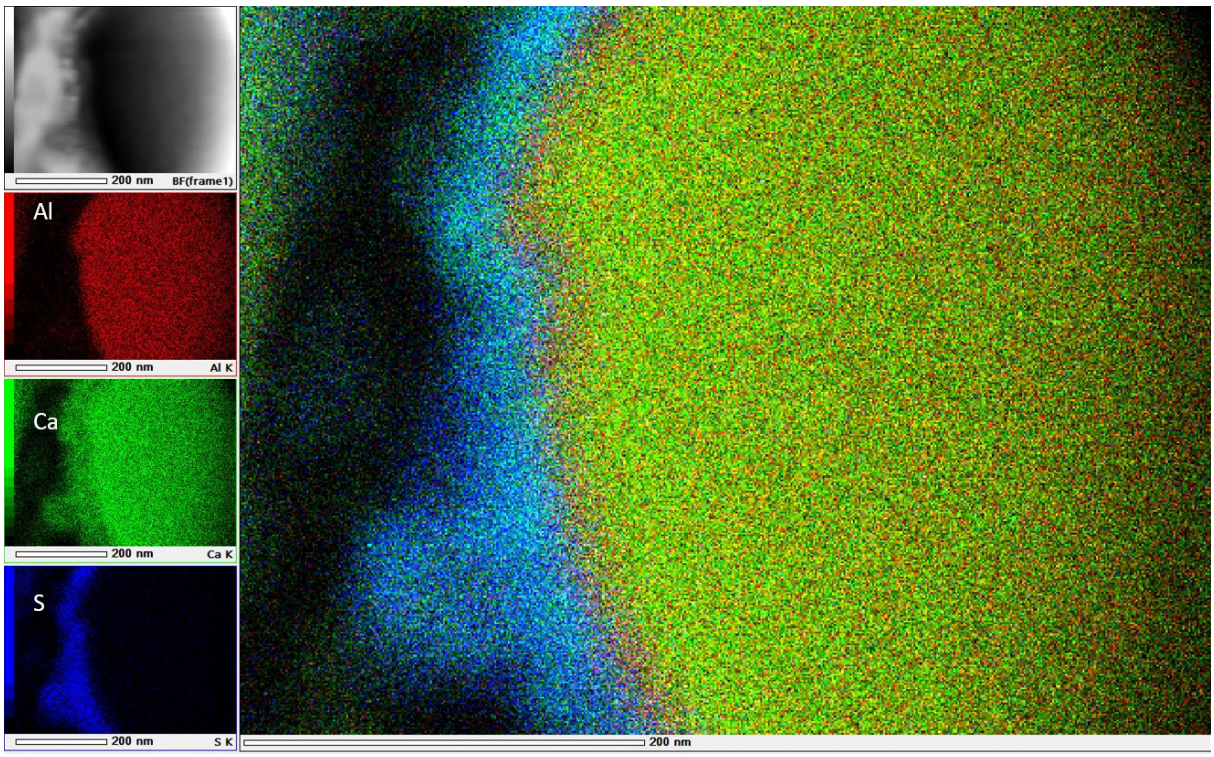

Figure 6. TEM-EDS element overlay map showing individual (left column) and combined maps for Al, Ca, and S. Scale = 200 nm. After Hood et al. [15].

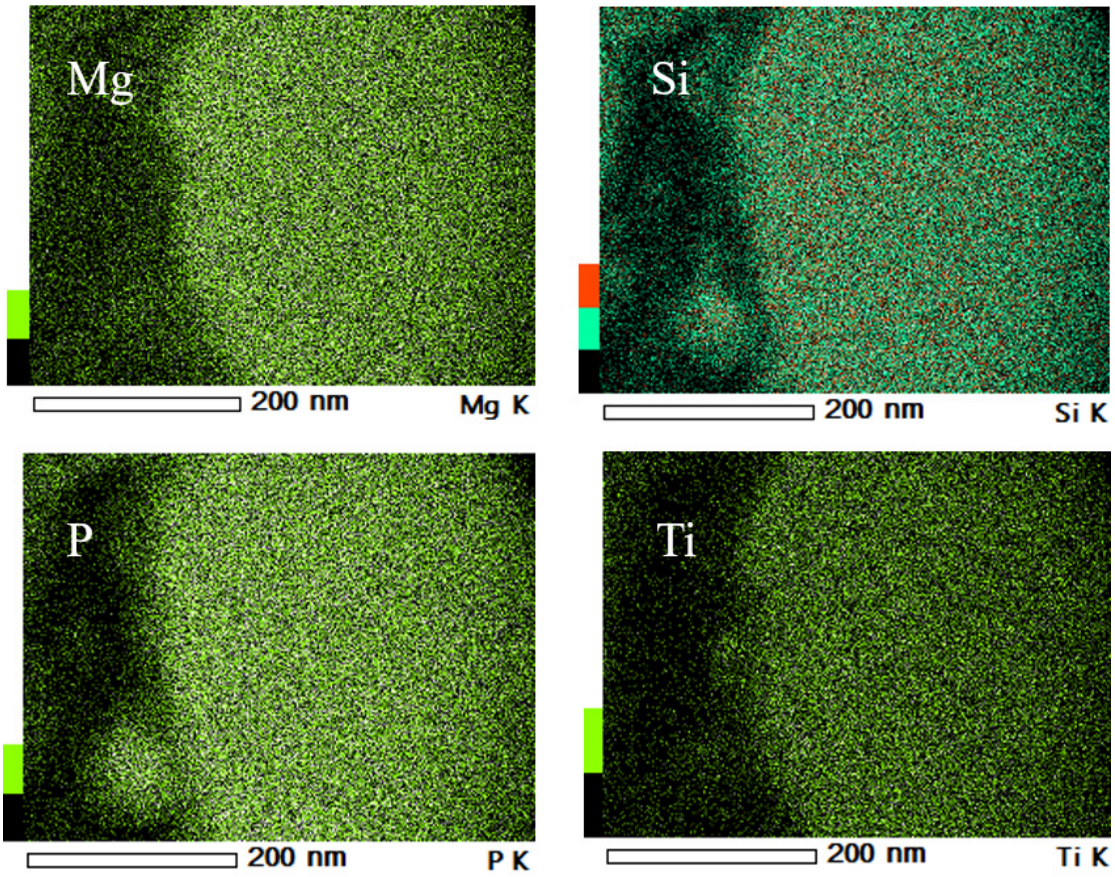

Figure 7. Distributions of Mg, Si, P, and Ti accompanying element map on Figure 6. Scale = 200 nm.

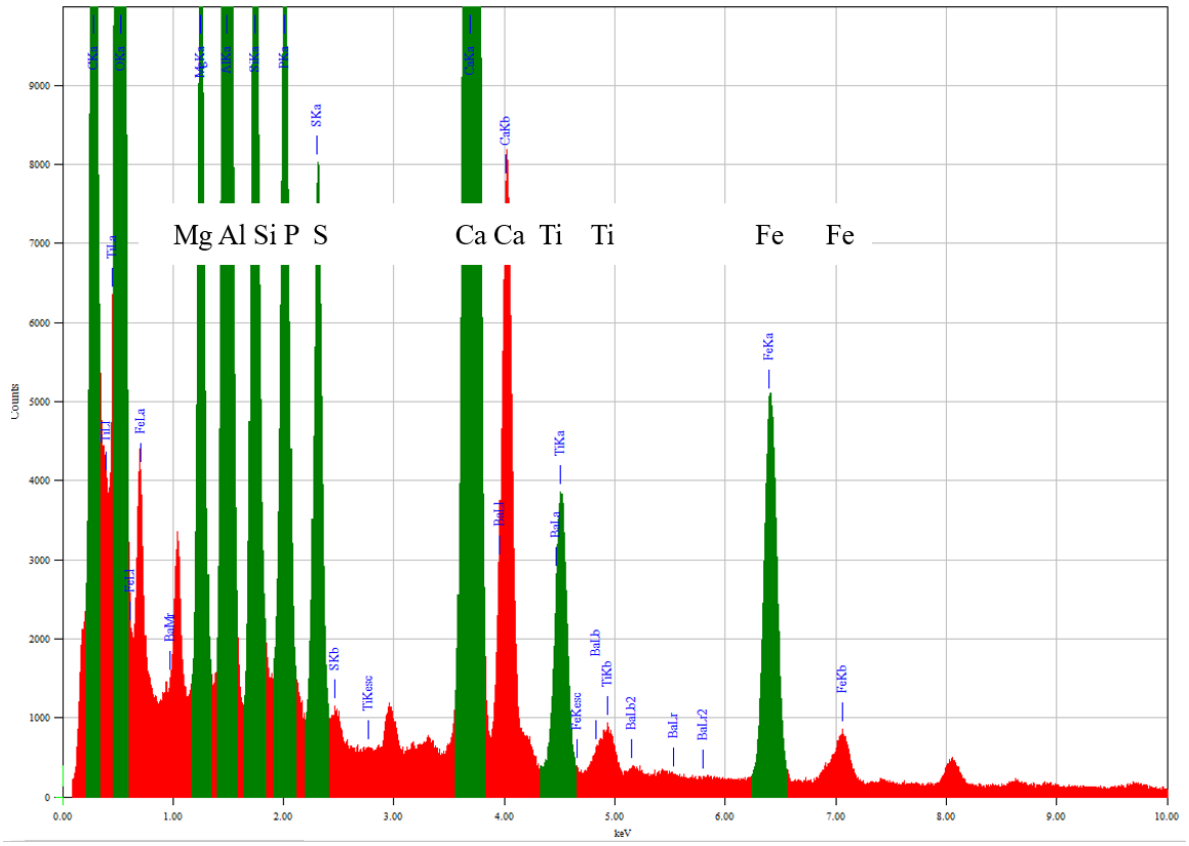

Figure 8. EDS spectrum accompanying Figures 6 and 7. Signals for Au and Pd (not labeled on this figure; see Figures 1 and 2) are extraneous to the sample. The green colored peaks have been used for mapping.

3.2.2. REE-Rich Particle: Analysis at University of Kentucky Electron Microscopy Center

Several REE-rich areas were examined in the particle shown on Figure 9. It is emphasized that, along with the particle shown on Figure 5, this is not a common find in this fly ash. The Figure 9 particle was selected following the preliminary SEM-EDS examination based on the promise of a diverse assemblage of REE-rich areas.

Areas 1213, 0940, and 1158/1201

Area 1213 is part of a larger area dominated by light REE but with some heavy REE and Y contributions (Figure 9). The high-angle annular dark-field (HAADF) image along with selected element maps is shown on Figure 10. In this example, La serves as a proxy for Ce and the other light REE and Er, along with Y, is a proxy for the heavy REE. The 0- to 10,000-eV range and the 4000- to 7500-eV REE range for area 1 within area 1213 is shown on Figure 11. In this case, the light REE and Gd show significant concentrations. Area 2, towards the upper edge of the particle (HAADF image on Figure 10), did not have significant concentrations of the REE.

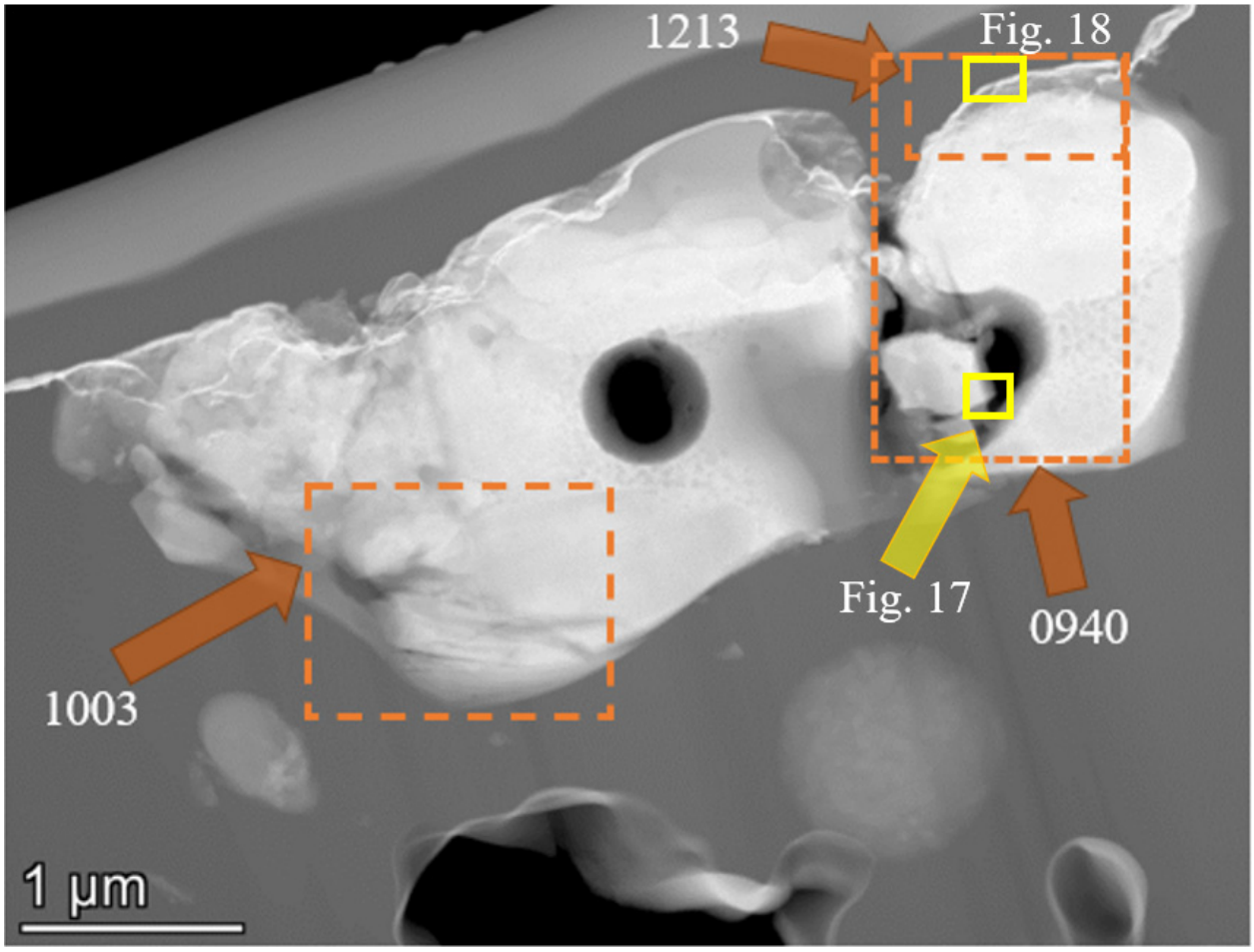

Figure 9. Areas 0940, 1213, and 1003 within a Y- and REE-rich fly ash particle. 1213 is within 940. The locations of Figures 17 and 18 are shown. HAADF (high-angle annular dark-field) image.

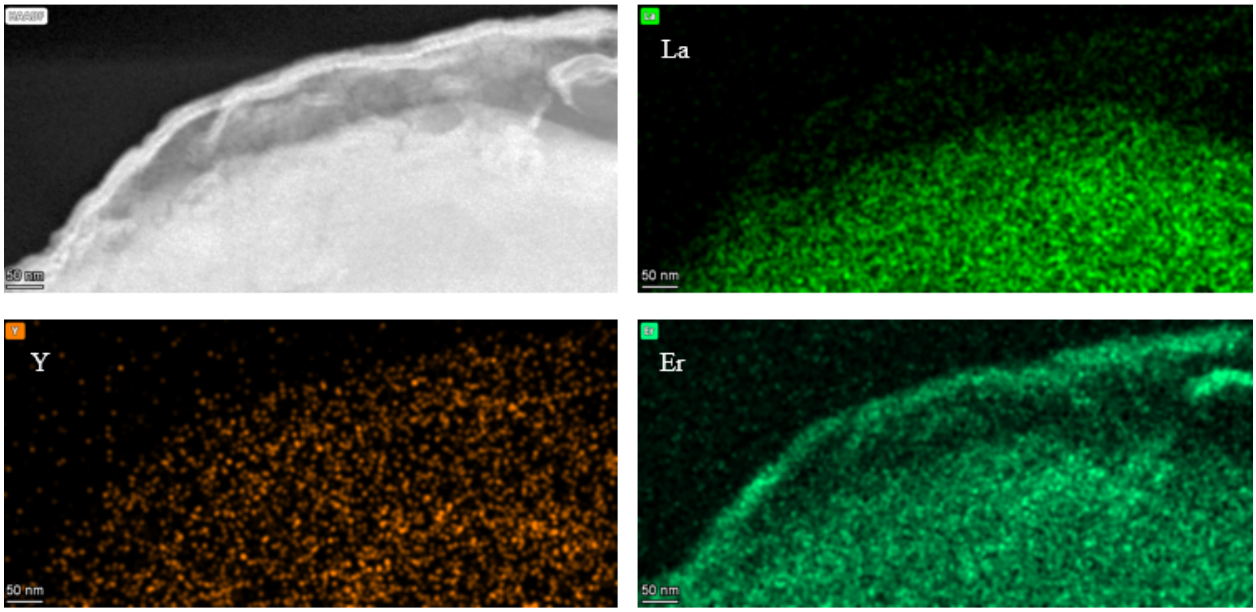

Figure 10. Area 1213. Clockwise from upper left: HAADF image; La element map; Er element map; and Y element map.

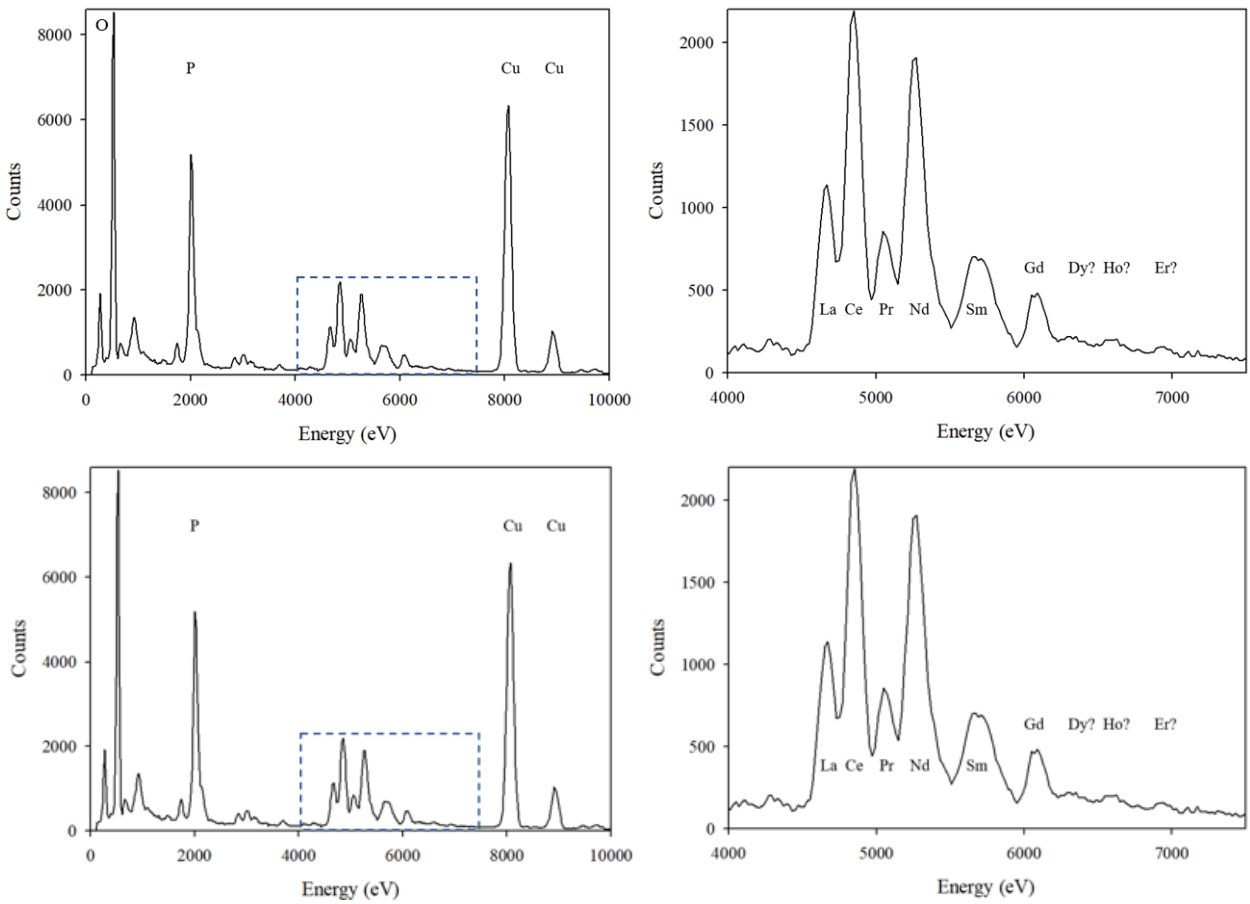

Figure 11. EDS for area 1 within area 1213. The full counts for the 0 to 10,000 eV range are shown on the (**left**) and a restricted count range for the 4000–7500 eV range is shown on (**right**) (dashed box on full-range figure indicates the area of the right figure). The Dy, Ho, and Er "peaks" do not represent significant concentrations of those elements. The Cu peak belongs to the grid holder, not the sample.

Area 0940, the larger area including and adjacent to area 1213 (inset on Figure 12 HAADF image), is generally dominated by light REE, represented by La, with lesser concentrations of Y and heavy REE, the latter represented by Dy (Figure 12). Yttrium and Dy are less dense in the truncated oval La-rich area on the right side, the rectangular particle in the upper-left quadrant, and in the lower left corner of Figure 12. Yttrium and, to a lesser degree, Dy and the other heavy REE, show their most evident concentrations in the region between the higher La concentrations (right side of the lower-left quadrant). On the HAADF image, the latter region shows up as a mottled area, a notably different texture compared to the flanking brighter areas. The mottling might represent few-nm crystals dispersed in the region or it could also be FIB re-deposition or FIB-induced damage, along with small crystallites present. The 0- to 10,000-eV range and the 4000- to 7500-eV REE range for area 3 within area 0940 is shown on Figure 13. Areas 1 and 2 have similar EDS spectra to Figure 13, but their Dy and Er "peaks" are even less significant than the Figure 13 peaks.

Area 1158 with magnified area 1201 (1158 inset on Figure 12) consists of a mottled region capped by whisker-like fine crystals (Figure 14).

Area 1003

The lower-left corner of the particle shown on Figure 9 contains at least three crystals of a P-Y-HREE-rich mineral (Figure 15). EDS (Figure 16) indicates that the mineral is a REE-rich mineral, possibly xenotime. The EDS spectra is unique in this study in showing significant concentrations of all of the even-number REE along with significant concentrations of most

of the heavy REE. The exceptions to the latter trend are the insignificant concentrations of Tb and Lu. While Y has an apparent presence on the element map (Figure 15), the proximity of the Y Lα and Lβ (1.924 and 1.998 keV, respectively) to the P Kα (2.010 keV) means that Y overlaps with P and can only be seen as a shoulder on the low-eV side of the P Kα. For all of the P-rich minerals in this study (xenotime and monazite are possible minerals, but not definitively identified), caution must be applied in interpreting, *and not over-interpreting*, apparent shows of Y (or any other element). The P- and LREE-rich (with La serving as the proxy for the light REE) "nose" above the latter crystals could not be specifically identified, but, from the chemistry, it would appear to be a LREE phosphate.

Fast Fourier Transform (FFT) Analysis of Mineralogy

Most of the attempts at using FFT in this study to determine the minerals of particles were not successful because the particles were too thick or because multiple nanometer-scale crystals with overlapping orientations did not yield usable results. The crystal in region 0940 (Figure 17; location on Figure 9) is an exception. The lattice interlayer spacings of 3.25 Å and 3.12 Å match those of the (200) crystal plane and (120) plane, respectively, of Cerium orthophosphate monazite, CePO4, with a monoclinic unit cell (JCPDS 32–0199), which is the most thermally stable cerium phosphate phase up to combustion temperatures (>1400 °C) [22,33]. In contrast, the region shown on Figure 18 (location on Figure 9) appears to be amorphous, with no crystalline lattice fringes and no diffraction spots in FFT.

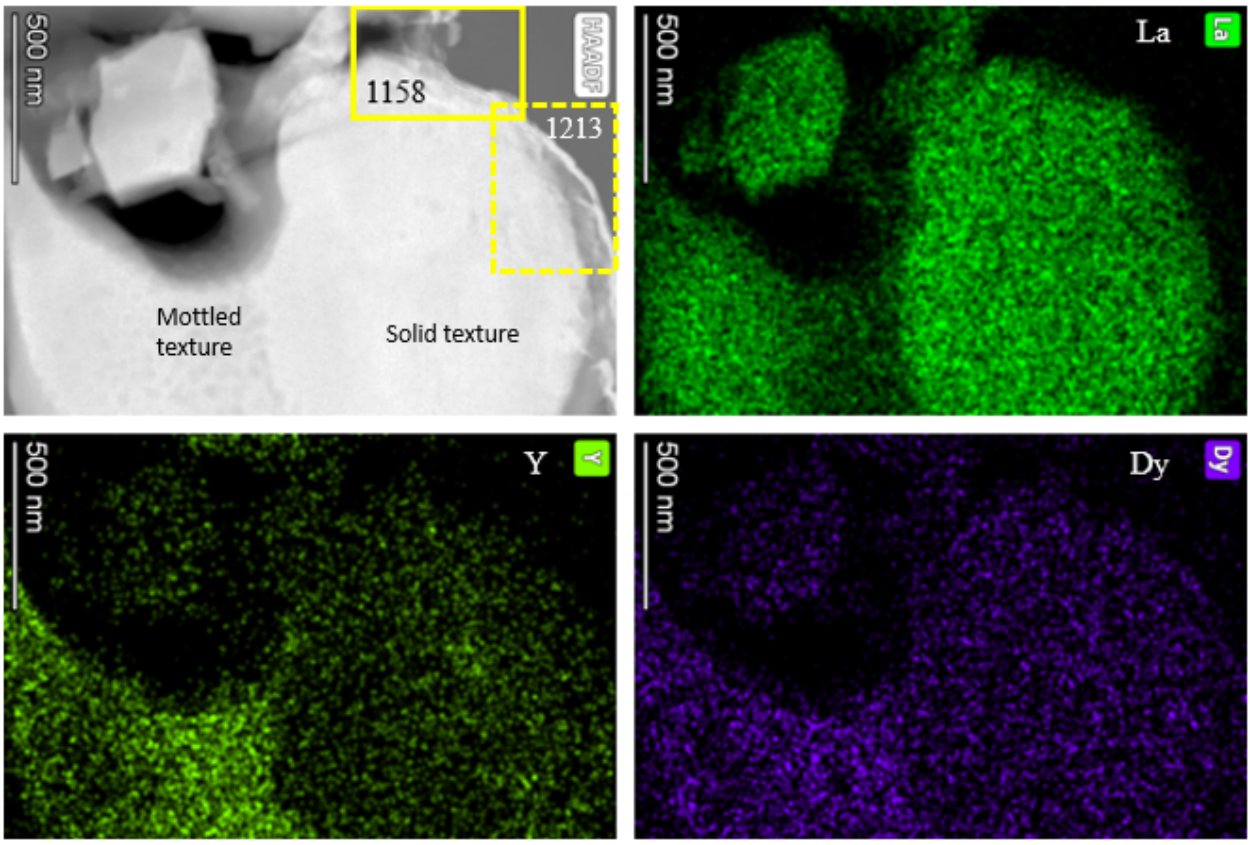

Figure 12. Area 0940. Clockwise from upper left: HAADF image of area with insets of areas 1213 (Figure 10) and 1158 (Figure 16); La element map; Dy element map; and Y element map.

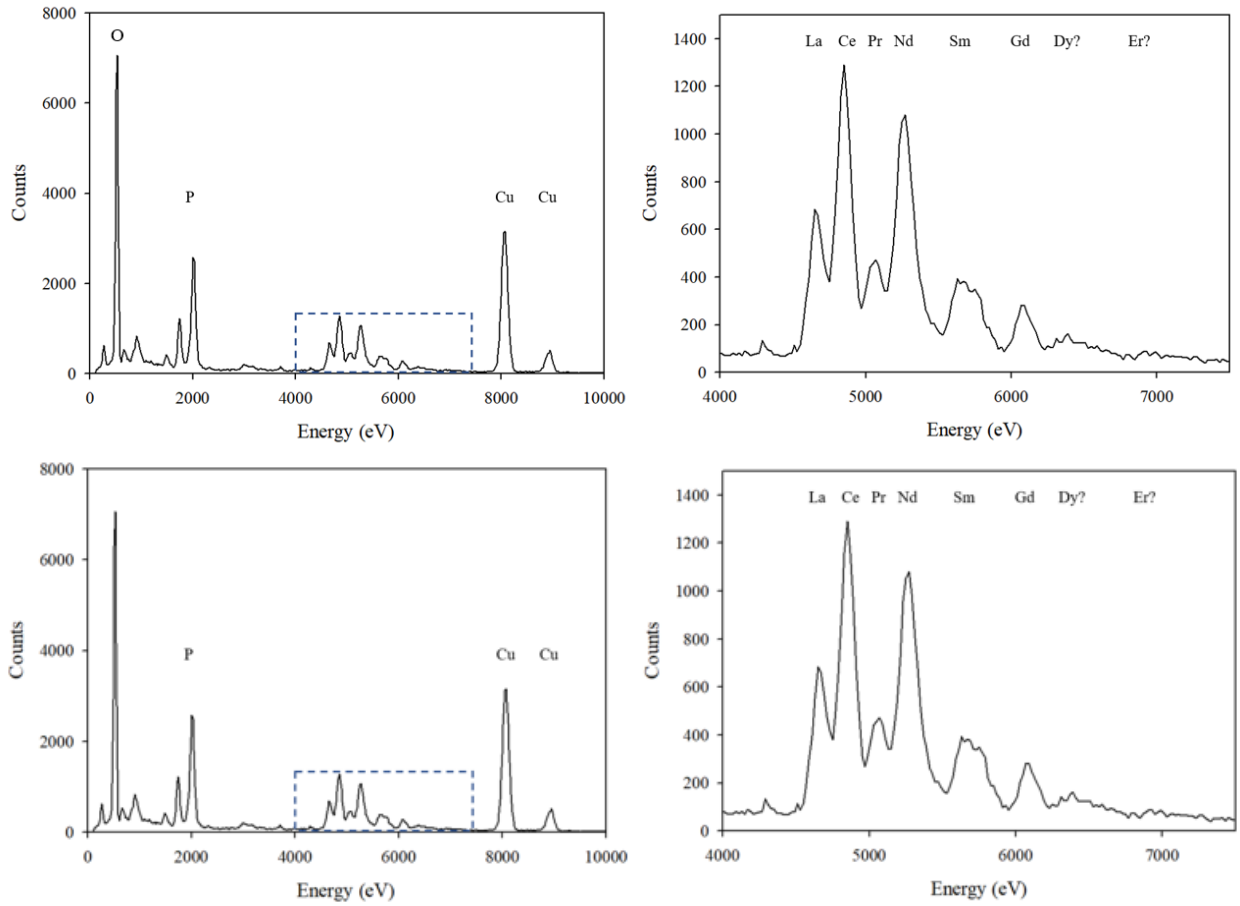

Figure 13. EDS for area 3 within area 0940. The full counts for the 0 to 10,000 eV range are shown on the left and a restricted count range for the 4000–7500 eV range is shown on right (dashed box on full-range figure indicates the area of the right figure). The Dy and Er "peaks" do not represent significant concentrations of those elements. The Cu peak belongs to the grid holder, not the sample.

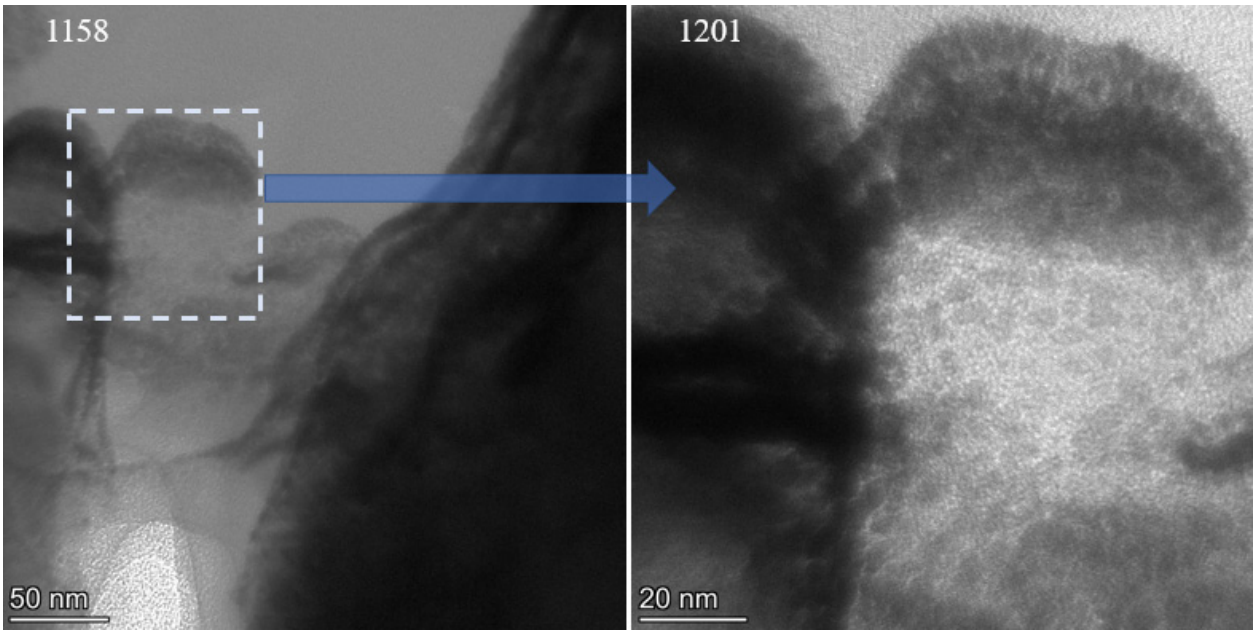

Figure 14. Area 1158 with inset shown for area 1201 (right).

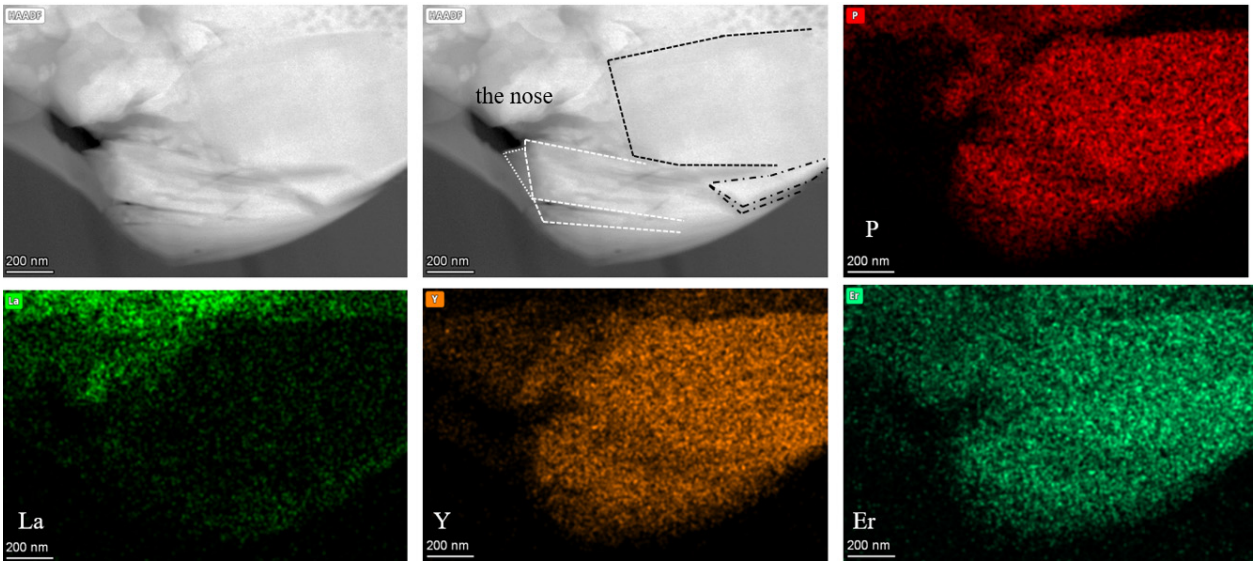

Figure 15. Area 1003. Clockwise from upper left: HAADF image of area; HAADF image with xenotime crystals outlined; P element map; Er element map; Y element map; La element map.

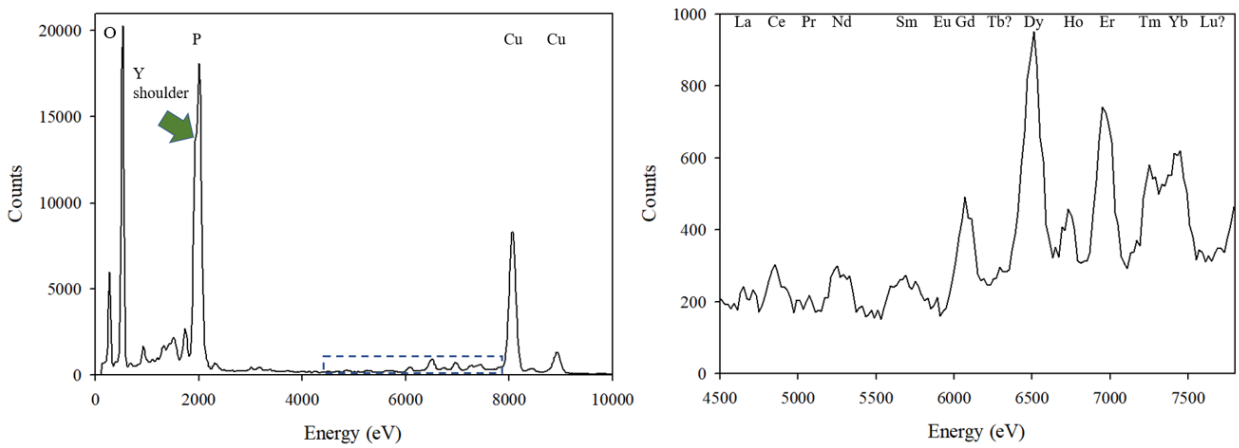

Figure 16. EDS for area 1 within area 1003. The full counts for the 0 to 10,000 eV range are shown on the left and a restricted count range for the 4500–7800 eV range is shown on right (dashed box on full-range figure indicates the area of the right figure). Yttrium appears as a shoulder on the P peak. The "peaks" for Eu, Tb, and Lu are not considered to be significant. The Cu peak belongs to the grid holder, not the sample.

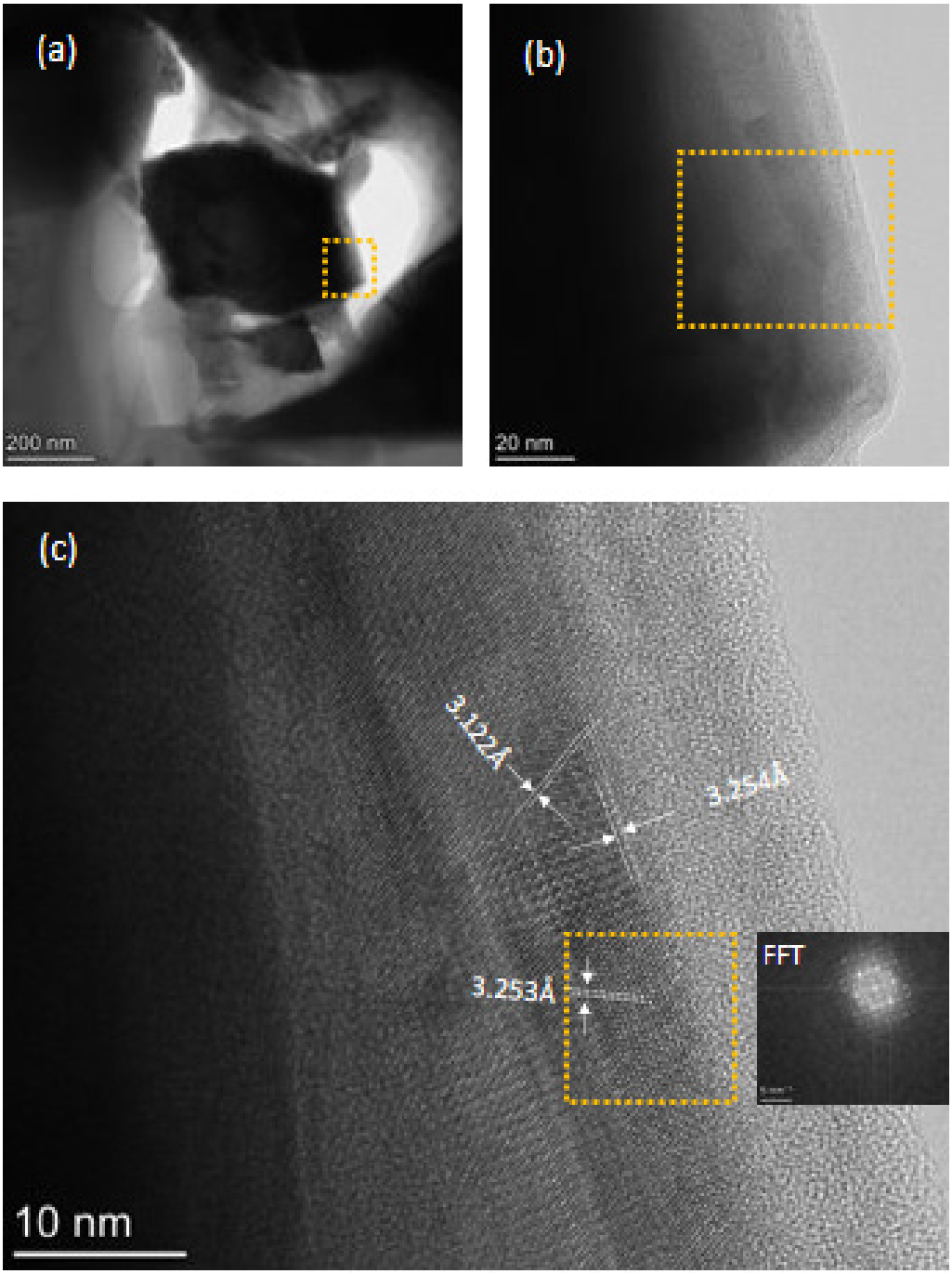

Figure 17. TEM image from STEM (Scanning TEM)-EDS region 0940 at low magnification (**a**,**b**) (scales = 200 nm and 20 nm, respectively) and high magnification (**c**) (scale = 10 nm). HRTEM image and the lattice interlayer space of the area blocked in STEM/EDS Region 0940.

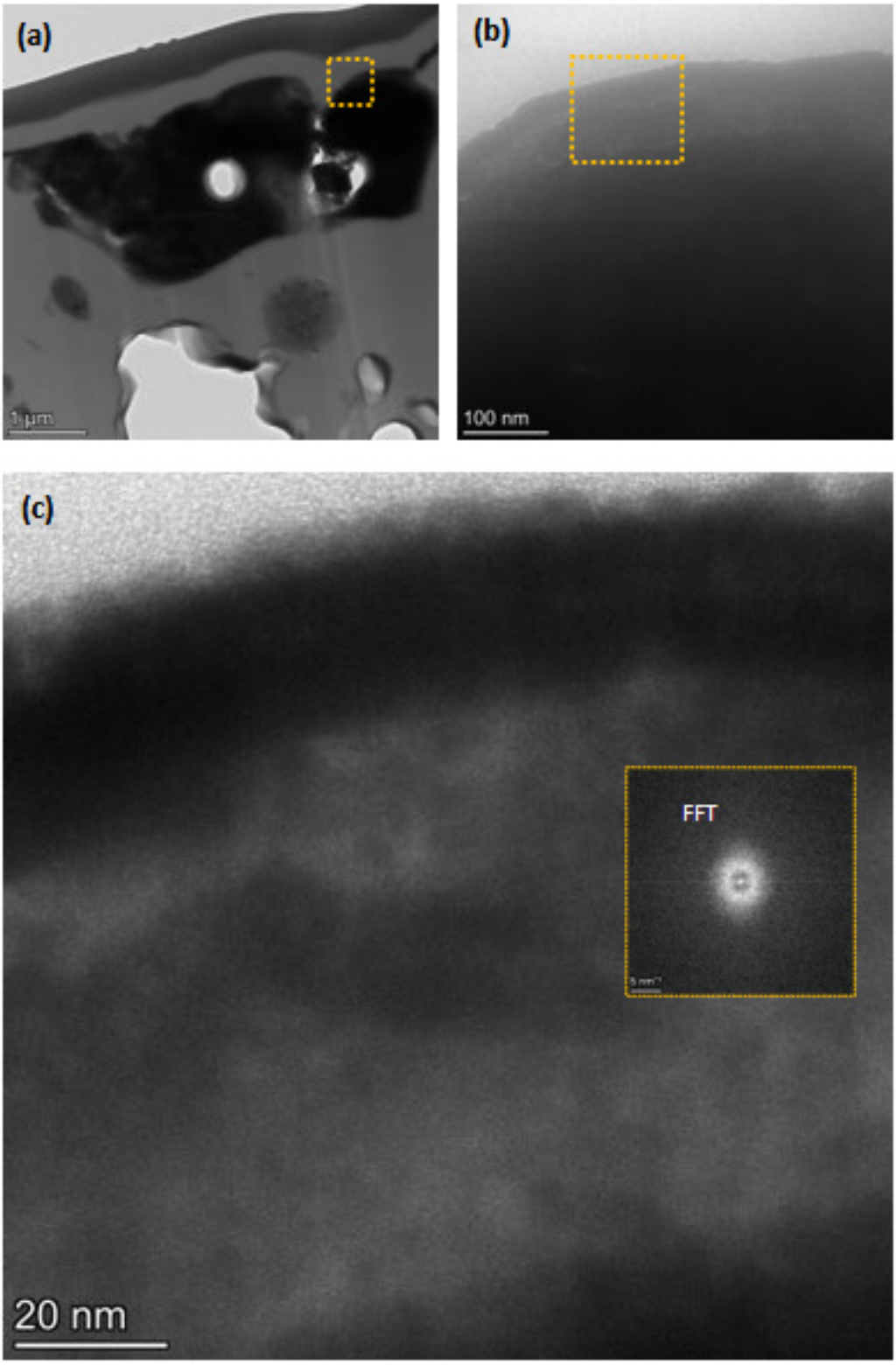

Figure 18. TEM image from STEM-EDS region 1213 at low magnification (**a**,**b**) (scales = 1 µm and 100 nm, respectively) and high magnification (**c**) (scale = 20 nm), shows no crystalline lattice fringes, therefore it is an amorphous phase. The absence of diffraction spots in FFT is shown in the inset of (**c**).

4. Summary

A fly ash derived from the combustion of a low-S, subbituminous Powder River Basin coal was examined by SEM-EDS and HRTEM-EDS with FFT also used in conjunction

with the HRTEM analysis. SEM-EDS shows the presence of a Ca-rich plagioclase feldspar (bytownite or anorthite), Mg-rich phases (diopside?), mixed Ca-Mg-Al-Si-Ti-Fe phases, and Ca-Si-Al phases. Of importance to the search for REE and other critical elements (Li, Ga, Ge, among others) in the fly ash, an Al ≈ Si > Ca > Ba > Mg > P ≈ Nd > Sm ≈ Fe particle was observed. The Ba Lα and Lβ peaks may be obscuring the La and Ce peaks and, considering the presence of Nd and Sm, it is possible that heavier REE may also be present.

HRTEM studies demonstrated the presence of mixed-composition amorphous particles (Ca > Al > >P ≈ Mg ≈ Si > S > Ti) rimmed by a Ca-S sulfate. Magnesium only follows the Ca distribution in the core of the particle, not the rim. Silicon and P follow the Ca-S distribution on the rim of the particle. HRTEM-EDS examination of mixed mineral and amorphous particles showed both LREE- and HREE-rich regions. Where the particles seem to be minerals, monazite appears to be the most likely LREE minerals and xenotime is among the possible HREE minerals.

Taggart et al. [14] demonstrated that, owing to the differences in the non-REE chemistry of the Class C PRB-derived ash compared to the Class F eastern US ashes examined in their study, the PRB-derived fly ashes had the potential for a greater percentage extraction of REE than the Appalachian- and Illinois Basin-derived fly ashes. In this study, a more comprehensive view of the association of REE within the PRB-derived fly ashes was obtained. In particular, the occurrence of heavy-REE-bearing minerals should be studied further. Along with the abundance of PRB-derived fly ash produced annually plus the several decades of ash produced, but not completely utilized, at several US coal-fired power plants, not all of them currently in operation, PRB-derived fly ash represents an abundant reserve of REE and, potentially, other critical elements.

Supplementary Materials: The following are available online at https://www.mdpi.com/article/10.3390/min12080975/s1, Table S1: Raw data for EDS spectra in areas 0925, 0940, 1003, and 1213.

Author Contributions: Conceptualization, J.C.H.; Formal analysis, J.C.H., D.B., C.R.W., D.Q. and N.J.B.; Funding acquisition, Dali Qian; Investigation, J.C.H.; Writing—original draft, J.C.H.; Writing—review and editing, D.B., C.R.W., D.Q., and N.J.B. All authors have read and agreed to the published version of the manuscript.

Funding: Portions of this study were completed as part of U.S. Department of Energy contracts DE-FE0026952, DE-FE0027167, and DE-FE0032053 and were further supported by National Science Foundation grant CBET-1510861 to the University of Kentucky. Access to characterization instruments and staff assistance was provided by the Electron Microscopy Center at the University of Kentucky, supported in part by the National Science Foundation/EPSCoR Award No. 1355438 and by the Commonwealth of Kentucky. This work used shared facilities at the Virginia Tech National Center for Earth and Environmental Nanotechnology Infrastructure (NanoEarth), a member of the National Nanotechnology Coordinated Infrastructure (NNCI), supported by NSF (ECCS 1542100 and ECCS 2025151).

Acknowledgments: We thank editors Scott Montross, Bruce Folkedahl, and Jonathan Yang for inviting us to participate in this Special Issue and we thank the editors and reviewers for the constructive comments on the manuscript.

Conflicts of Interest: The authors declare no conflict of interest.

References

1. U.S. Environmental Protection Agency. Sulfur Dioxide (SO_2) Pollution. 2021. Available online: https://www.epa.gov/so2-pollution (accessed on 8 June 2022).
2. U.S. Environmental Protection Agency. Mercury. 2022. Available online: https://www.epa.gov/mercury (accessed on 8 June 2022).
3. Vaninetti, G.E.; Worrall, C. Markets for southern Powder River Basin coal. *Min. Eng.* **1994**, *46*, 951–954.
4. Young, B.C.; Pavlish, J.H.; Gerlach, T.R.; Zygarlicke, C.J. Mitigation of air toxic elements from the combustion of low-rank coals in power generation plants. In Proceedings of the Air & Waste Management Association's Annual Meeting & Exhibition, Nashville, TN, USA, 23–28 June 1996; p. 18.
5. Schimmoller, B.K. Western push east. *Power Eng.* **1999**, *103*, 18–26.
6. Buecker, B.; Meinders, J. PRB coal switch not a complete panacea. *Power Eng.* **2000**, *104*, 76–79.
7. Benson, S.A. How does Western coal affect mercury emissions? *EM: Air Waste Manag. Assoc. Mag. Environ. Manag.* **2003**, 32–34. Available online: https://www.osti.gov/etdeweb/biblio/20423883 (accessed on 29 July 2022).
8. Javetski, J. Burning PRB coal: Problems and solutions. *Power* **2004**, *148*, 46–50.
9. Medine, E.S.; Schwartz, S. The roller coaster formerly known as the PRB. *Coal Age* **2006**, *111*, 34–35.
10. Gerking, S.; Hamilton, S.F. What explains the increased utilization of Powder River Basin coal in electric power generation? *Am. J. Agric. Econ.* **2008**, *90*, 933–950. [CrossRef]
11. Deye, C.S.; Layman, C.M. A review of Electrostatic Precipitator upgrades and SO_2 reduction at the Tennessee Valley Authority Johnsonville Fossil Plant. In *Air and Waste Management Association-7th Power Plant Air Pollutant Control 'Mega' Symposium*; Air Waste Management Association: Pittsburgh, PA, USA, 2008; Volume 2, pp. 1056–1073.
12. Chudnovsky, B.; Talanker, A.; Berman, Y.; Saveliev, R.; Perelman, M.; Korytnyi, E.; Davidson, B.; Bar-Ziv, E. *Prediction of Performance from PRB Coal Fired in Utility Boilers with Various Furnace and Firing System Arrangements*; American Society of Mechanical Engineers, Power Division (Publication) PWR: New York, NY, USA, 2009; pp. 27–34.
13. McCartney, R.H.; Williams, R.L., Jr. Fuel blending with PRB coal. *Power Eng.* **2009**, *113*, 54–60.
14. Taggart, R.K.; Hower, J.C.; Dwyer, G.S.; Hsu-Kim, H. Trends in the rare-earth element content of U.S.-based coal combustion fly ashes. *Environ. Sci. Technol.* **2016**, *50*, 5919–5926. [CrossRef]
15. Hood, M.M.; Taggart, R.K.; Smith, R.C.; Hsu-Kim, H.; Henke, K.R.; Graham, U.M.; Groppo, J.G.; Unrine, J.M.; Hower, J.C. Rare earth element distribution in fly ash derived from the Fire Clay coal, Kentucky. *Coal Combust. Gasif. Prod.* **2017**, *9*, 22–33. [CrossRef]
16. Bagdonas, D.A.; Nye, C.; Thomas, R.B., Sr.; Rose, K.K. Rare earth element occurrence and distribution in Powder River Basin coal core, Wyoming. In Proceedings of the 36th Annual International Pittsburgh Coal Conference: Clean Coal-Based Energy/Fuels and the Environment, Pittsburgh, PA, USA, 3–6 September 2019.
17. Hower, J.C.; Groppo, J.G.; Henke, K.R.; Graham, U.M.; Hood, M.M.; Joshi, P.; Preda, D.V. Ponded and landfilled fly ash as a source of rare earth elements from a Kentucky power plant. *Coal Combust. Gasif. Prod.* **2017**, *9*, 1–21. [CrossRef]
18. Hower, J.C.; Groppo, J.G.; Joshi, P.; Preda, D.V.; Gamliel, D.P.; Mohler, D.T.; Wiseman, J.D.; Hopps, S.D.; Morgan, T.D.; Beers, T.; et al. Distribution of Lanthanides, Yttrium, and Scandium in the pilot-scale beneficiation of fly ashes derived from eastern Kentucky coals. *Minerals* **2020**, *10*, 105. [CrossRef]
19. Hower, J.C.; Groppo, J.G.; Hsu-Kim, H.; Taggart, R.K. Signatures of Rare Earth Element distributions in fly ash derived from the combustion of Central Appalachian, Illinois, and Powder River basin coals. *Fuel* **2021**, *301*, 121048. [CrossRef]
20. Hower, J.C.; Groppo, J.G.; Jewell, R.F.; Wiseman, J.D.; Duvallet, T.Y.; Oberlink, A.E.; Hopps, S.D.; Morgan, T.D.; Henke, K.R.; Joshi, P.; et al. Distribution of Rare earth elements in the pilot-scale processing of fly ashes derived from eastern Kentucky coals: Comparisons of the feed and processed ashes. *Fuel* **2021**, *295*, 120562. [CrossRef]
21. ASTM International. *Standard Specification for Coal Fly Ash and Raw or Calcined Natural Pozzolan for Use in Concrete*; ASTM C618-19; ASTM International: West Conshohoken, PA, USA, 2019.
22. Hower, J.C.; Qian, D.; Briot, N.; Henke, K.R.; Hood, M.M.; Taggart, R.K.; Hsu-Kim, H. Rare earth element associations in the Kentucky State University stoker ash. *Int. J. Coal Geol.* **2018**, *189*, 75–82. [CrossRef]
23. Hower, J.C.; Qian, D.; Briot, N.J.; Santillan-Jimenez, E.; Hood, M.M.; Taggart, R.K.; Hsu-Kim, H. Nano-scale rare earth distribution in fly ash derived from combustion of the Fire Clay coal, Kentucky. *Minerals* **2019**, *9*, 206. [CrossRef]
24. Hower, J.C.; Cantando, E.; Eble, C.F.; Copley, G.C. Characterization of stoker ash from the combustion of high-lanthanide coal at a Kentucky bourbon distillery. *Int. J. Coal Geol.* **2019**, *213*, 103260. [CrossRef]
25. ASTM International. *Ultimate Analysis of Coal and Coke, ASTM D3176-15*; ASTM International: West Conshohoken, PA, USA, 2015.
26. French, D.; Dale, L.; Matulis, C.; Saxby, J.; Chatfield, P.; Hurst, H.J. Characterization of mineral transformations in pulverized fuel combustion by dynamic high-temperature X-ray diffraction analysis. In Proceedings of the 18th Pittsburgh International Coal Conference, Newcastle, Australia, 3–7 December 2001; p. 7.
27. Osborn, E.F.; Muan, A. Phase equilibrium diagrams of oxide systems. In *The System CaO-Al_2O_3-SiO_2. Plate 1*; The American Ceramic Society and the Edward Orton Jr. Ceramic Foundation: Columbus, OH, USA, 1960.
28. Ehlers, E.G. *The Interpretation of Geological Phase Diagrams*; W.H. Freeman & Co.: San Francisco, CA, USA, 1972; p. 280.
29. Alekseev, Y.I.; Vereshchagin, V.I. Formation of crystalline phases in electroceramics of the system $CaO-MgO-Al_2O_3-SiO_2$ (A review). *Glass Ceram.* **1997**, *54*, 340–343. [CrossRef]

30. Schairer, J.H.; Yoder, H.S., Jr. The system albite-anorthite-forsterite at 1 atmosphere. *Yearb. Carnegie Inst. Wash.* **1967**, *65*, 204–209.
31. Querol, X.; Fernandez Turiel, J.L.; Lopez Soler, A. The behaviour of mineral matter during combustion of Spanish subbituminous and brown coals. *Mineral. Mag.* **1994**, *58*, 119–133. [CrossRef]
32. Hower, J.C.; Henke, K.R.; Dai, S.; Ward, C.R.; French, D.; Liu, S.; Graham, U. The generation and nature of coal fly ash and bottom ash. In *Coal Combustion Products*; Robl, T.L., Oberlink, A., Jones, R., Eds.; Woodhead Publishing (Elsevier): Cambridge, MA, USA, 2017; Volume 2, pp. 21–65. [CrossRef]
33. Ray, H.L.; Zhao, N.; De Jonghe, L.C. Hole percolation and proton conduction in monazite solid solutions: La 0.98-xCe xSr 0.02PO 4-δ. *Electrochim. Acta* **2012**, *78*, 294–301. [CrossRef]